Plasma-Induced Electronic Defects: Generation and Annihilation Kinetics in Hydrogenated Amorphous Silicon

Shota Nunomura,* Isao Sakata, and Koji Matsubara

Research Center for Photovoltaics, National Institute of Advanced Industrial Science and Technology, 1-1-1 Umezono, Tsukuba, Ibaraki 305-8568, Japan

(Received 29 May 2018; revised manuscript received 12 September 2018; published 2 November 2018)

Plasma processing is a key technology for fabrication of state-of-the-art semiconductor devices. The device performance is often limited by electronic defects generated during plasma processing, although most of those defects are annihilated by postannealing. Here we experimentally study the defect kinetics in hydrogenated amorphous silicon (*a*-Si:H) during hydrogen- (H_2-) and argon- (Ar-) plasma treatment, and also consecutive postannealing. The generation and annihilation of electronic defects such as silicon dangling bonds are monitored via *in situ* measurements of the photocurrent. From the measurements, the following results are found: (i) The defects are generated dominantly by radical species such as H atoms for a H_2 plasma and metastable Ar atoms for an Ar plasma. (ii) The Ar^+-ion bombardment creates residual defects, whereas the H_3^+-ion bombardment does not create such defects. The residual defects are mostly recovered by an additional H_2-plasma and postannealing treatment. (iii) The annihilation of defects exhibits stretched exponential behavior, revealing the dispersive nature of *a*-Si:H. (iv) The activation energy for the annihilation of defects depends on the origins of the defect generation. The activation energy is smaller for defects generated by plasma treatments compared with that for defects induced by photon irradiation. A rate equation for the generation and annihilation of defects is described, and the defect kinetics is discussed in terms of microstructural changes associated with hydrogen diffusion.

DOI: 10.1103/PhysRevApplied.10.054006

I. INTRODUCTION

Electronic defects in semiconductor devices play important roles in the device performance and reliability [1,2]. For example, the electronic defects in field-effect transistors often induce a leakage current and/or a threshold-voltage shift, leading to performance degradation [3–6]. In silicon-heterojunction solar cells [7,8], the defects behave as the recombination centers for photogenerated carriers, so the power-conversion efficiency is lowered. These defects are often generated during device fabrication, where a variety of plasma-processing steps are used for thin-film deposition, etching, dopant implantation, and surface modification [3,4,9–11]. Most of the defects are recovered or annihilated by postannealing treatment. However, some defects remain in devices, restricting the device performance.

During plasma processing, the electronic defects can be generated near the material surface for several reasons [3,4,9–11], shown schematically in Fig. 1. The material surface is exposed to ion bombardment, photon irradiation, radicals, particulate attachment, and charging. Ion bombardment may lead to surface strain and loss of matter by sputtering events, which results in the formation of defects near the surface [12–15]. Some energetic ions may penetrate into certain materials, where they are neutralized and behave as impurities. Photon irradiation generates dangling bonds (DBs) by breaking the weak bonds in materials [16–19]. Radical exposure is expected to generate defects by transferring the internal energy to the surface atoms and/or radicals chemically reacting with the lattice atoms [20–23]. Particulates or dusts can be deposited on the surface in deposition processes, which results in voids or pores accompanied by defects [24,25]. Surface charging may cause an electrical breakdown, associated with the formation of defects in insulating materials [10].

The electronic defects formed via plasma processing can be detected by a variety of *ex situ* methods [2,26]: capacitance-voltage measurement [2,27,28], deep-level transient spectroscopy [2,28,29], electron spin resonance (ESR) [30,31,33], constant-photocurrent measurement [34–37], X-ray photoelectron spectroscopy [38,39], and other methods [2,26]. These methods are useful for characterizing the electronic states formed by defects (i.e., the density of states in the band gap) [40,41]. However, the information provided by these measurements is limited when the measurement is performed outside the processing environment (i.e., a plasma). On the other hand, only a few methods have been developed for *in situ* detection of electronic defects. One example is

*s.nunomura@aist.go.jp

 © 2018 American Physical Society

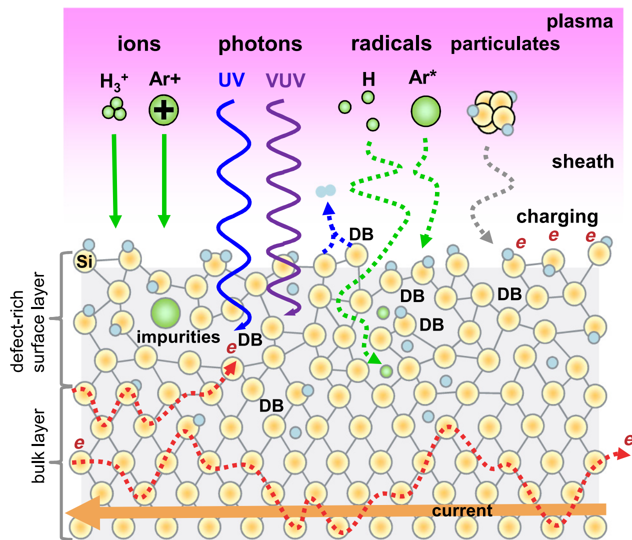

FIG. 1. Electronic defects and carrier transport in a a-Si:H film during plasma processing. Electronic defects such as DBs are generated by ion bombardment, photon irradiation, radical exposure, particulate attachment, and surface charging. The defects are distributed in a defect-rich surface layer, where weak Si—H and Si—Si bonds are broken and the local structure is disturbed. The carrier (electron) transport is highly limited in this layer, denoted by a zigzag line in the middle left. Underneath this, the bulk layer is located, where the local structure is intact. The carriers are transported mainly through this layer, denoted by a zigzag line in the lower part.

the time-resolved-microwave-conductivity method, which was used to monitor the surface defects on crystalline silicon wafers [44,45]. Another is evanescent-wave cavity ring-down spectroscopy, which was used to study the dangling-bond defects in thin-film materials [46,47]. However, the generation and annihilation of electronic defects during plasma processing and consecutive postannealing have not been systematically studied so far.

In this paper, we study the defect kinetics in hydrogenated amorphous silicon (a-Si:H) films during plasma treatment and postannealing. The generation and annihilation of electronic defects such as silicon dangling bonds are monitored via *in situ* measurements of the photocurrent [48,49]. The method for defect monitoring is described in Sec. II, and the experimental procedures are explained in Sec. III [48–50]. The dominant species responsible for the generation of defects is distinguished by the experiments, where the film surface is selectively exposed to photons, radicals, and ions (Sec. IV) [51,52]. The annihilation of defects is observed during the postannealing, and the activation energy is determined from an Arrhenius plot (Sec. IV E). The mechanism for the generation and annihilation of defects is discussed from a microstructural point of view (Sec. V). A possible mechanism for the creation of residual defects by ion bombardment is also discussed. Finally, we present our conclusions in Sec. VI.

Among a wide variety of semiconductor materials, in this study we select a-Si:H, which is one of the most-widely-used semiconductor materials; it is used as an active layer in thin-film transistors, an absorber in a-Si:H solar cells [40,41], and a passivation layer in silicon-heterojunction solar cells [7,8]. The electronic properties of a-Si:H films have been well investigated [40,41]. According to earlier studies, the density of states related to electronic defects is classified into two groups: the deep-level and the shallow-level states, as shown in Fig. 2(a). The deep-level states primarily originate from the DBs. These states are located roughly 0.6 eV below the conduction-band edge, so they behave as the recombination centers. The lifetime of the minority carriers is limited by these states [Fig 2(b)]. The density of the deep-level states is on the order of 10^{15}–10^{16} cm^{-3}. In this study, we focus on this group of electronic defects, (i.e., the deep-level states originating from DBs). The origins of the deep-level states are not completely resolved. The defects associated with nanoporous structure may be another possible candidate for the deep-level states [42,43]. On the other hand, the shallow-level states come from the distribution of the bond lengths and angles (i.e., the disordering of the a-Si:H network structure). The density of these states decreases exponentially from the conduction-band and valence-band edges. These states behave as the trap

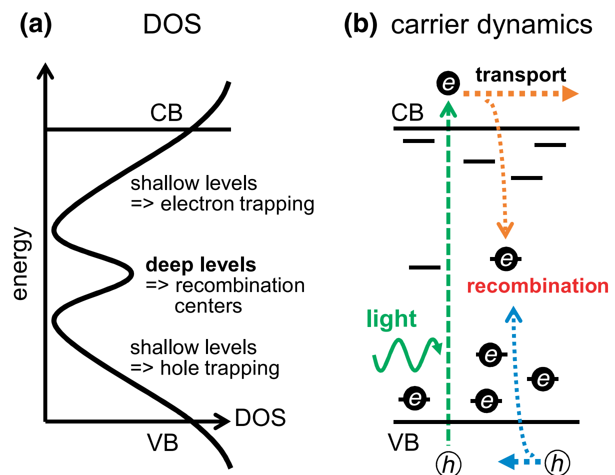

FIG. 2. (a) Density-of-states (DOS) distribution in a-Si:H. It consists of two groups: the shallow-level states and the deep-level states. The shallow-level states, related to the deformation of bonds, are located near the conduction band (CB) and the valence band (VB). The deep-level states, associated with DBs, are located near the midgap. (b) Carrier dynamics. Light illumination induces the generation of photocarriers in a-Si:H. The photocarriers are trapped in the deep-level states during transport, which results in the recombination of carriers.

sites for carriers, such that the carrier mobility is influenced by the distribution of these states.

II. METHOD FOR DEFECT MONITORING

The generation and annihilation of defects can be monitored via the measurement of the photocurrent [48,49]. The photocurrent is primarily proportional to the carrier mobility-lifetime product ($I_p \propto \mu\tau$) [53,54], where the carrier lifetime is inversely proportional to the density of recombination centers [2]; that is deep-level defect states associated with DBs in *a*-Si:H ($\tau \propto 1/n_d$). So, the photocurrent, I_p, is a function of the defect density, n_d, as follows:

$$I_p \propto 1/n_d. \tag{1}$$

Here the film thickness and the photocarrier-generation rate are assumed to be constant. In Eq. (1), a decrease in the photocurrent reflects the generation of defects, whereas an increase in the photocurrent reflects the annihilation of defects.

Because the photocurrent intensity strongly depends on the defect density, defect monitoring based on photocurrent measurement is highly sensitive to a small amount of defects, which would not be detected by optical methods such as Fourier-transform IR spectroscopy and spectroscopic ellipsometry. However, this technique does not give an absolute value of the defect density. Another characterization is required to determine it; for instance, deep-level transient spectroscopy [2,28,29] and ESR [30–33] measurements are often used.

The carrier mobility also influences a change of the photocurrent. This effect is, however, negligible for a thick *a*-Si:H film with plasma treatment. The carrier mobility is a parameter related to the bulk property, while plasma treatment is considered to induce microstructural changes near the surface.

III. EXPERIMENTAL PART

A. Sample preparation

We prepare undoped intrinsic *a*-Si:H films on glass substrates (Corning Eagle XG, 0.5 mm thick) by means of plasma-enhanced chemical vapor deposition [56]. Before the deposition, interdigitated contacts are formed on the glass substrates for the photocurrent measurement. The contacts are made of 200-nm-thick Ag, covered with 40-nm-thick Ga-doped ZnO, which yields an Ohmic contact to a *a*-Si:H film. The interdigitated structure yields 19 channels for the photocurrent path. Each channel is 0.2 mm long and 5 mm wide.

Plasma-enhanced chemical vapor deposition is performed in a capacitively coupled 60-MHz very-high-frequency (VHF) discharge of hydrogen (H_2) and silane (SiH_4) gas mixture [57,58]. The *a*-Si:H films are deposited under the following conditions: a deposition temperature

TABLE I. Discharge conditions for *a*-Si:H deposition and H_2- and Ar-plasma treatments.

	a-Si:H deposition	H_2-plasma treatment	Ar-plasma treatment
Temperature T (°C)	200	120–240	200
Pressure p (Torr)	0.3	0.3	0.3
H_2 flow rate (sccm)	50	50	0
Ar flow rate (sccm)	0	0	50
SiH_4 flow rate (sccm)	10	0	0
Discharge power (W)	5	3–50	3–50
Discharge/treatment time $\Delta t(s)$	1030	60	2–1000

of 200 °C, a discharge power of 39 mW/cm^2, a gas pressure of 0.3 Torr, and a H_2-to-SiH_4 gas flow ratio of 5. The film thickness is controlled to be $d = 220 \pm 5$ nm by adjustment of the discharge period. These conditions are listed in Table I. Such conditions yield device-grade *a*-Si:H for solar-cell applications [59,60].

After the deposition, we characterize optoelectronic properties of the *a*-Si:H films at room temperature in air. The band gap, the refractive index, and the extinction coefficient at wavelength $\lambda = 520$ nm are determined by spectroscopic ellipsometry [61] under the assumption of a Tauc-Lorentz model [62]: $E_g = 1.70$ eV, $n_{520} = 4.62$, and $k_{520} = 0.43$, respectively. The defect density (i.e., the density of the deep-level states originating from DBs in the intrinsic *a*-Si:H) is obtained from ESR. The ESR spin density is on the order of 10^{15} cm^{-3} [63]. The Urbach energy, characterizing the distribution of the shallow-level states, is determined by constant-photocurrent measurement; it is $E_U = 46 \pm 2$ meV [59,60].

We prepare four different structures of samples by placing glass or quartz over the deposited *a*-Si:H film, as shown in Fig. 3 [51,52]; these are referred to as samples A, B, C, and D. Sample A is an uncovered *a*-Si:H film, and the film is therefore exposed to ions, radicals, and photons generated by the plasma. Sample B is a *a*-Si:H film covered with glass and with a gap of 0.5 mm between the *a*-Si:H film and the glass. The inclusion of the glass eliminates ion bombardment on the *a*-Si:H film, while the gap between the *a*-Si:H and the glass allows radicals to reach the *a*-Si:H film. Since the glass transmits photons with energy $h\nu$ below approximately 5.0 eV (i.e., $\lambda \gtrsim 250$ nm), the *a*-Si:H film is exposed to photons in the spectral range from ultraviolet (UV) to visible light. Sample C is a *a*-Si:H film covered with glass and sealed completely with ceramic paste (i.e., the gap between the *a*-Si:H and the glass is closed). This prevents exposure of the *a*-Si:H film to radicals, and the film is therefore exposed to only UV and visible photons. Sample D is a *a*-Si:H film covered with quartz glass and sealed with ceramic paste. The quartz transmits photons with energy $h\nu$ up to approximately 7.3

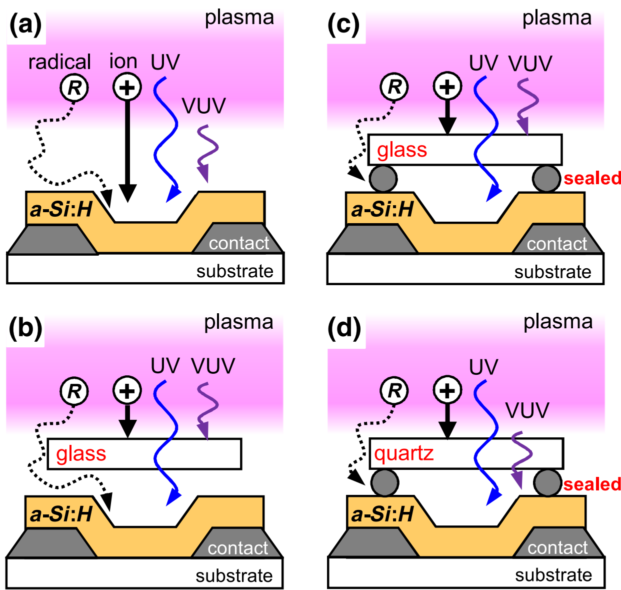

FIG. 3. Sample structures. A a-Si:H film is deposited on a glass substrate with contacts. (a) Sample A. A a-Si:H film is uncovered. The film is exposed to ions, radicals, and photons, coming from a plasma. (b) Sample B. A a-Si:H film is covered with glass with a small gap. Ion bombardment over the film is prevented. The film is exposed to radicals and photons in the range from UV to visible light. (c) Sample C. A a-Si:H film is covered with glass and sealed completely with ceramic paste. The penetration of radical species is prevented. The film is exposed to the UV and visible photons. (d) Sample D. A a-Si:H film is covered with quartz glass and sealed with ceramic paste. The film is exposed to VUV photons.

eV (i.e., $\lambda \gtrsim 170$ nm), and therefore the a-Si:H film is exposed to visible, UV, and vacuum-UV (VUV) photons.

B. Hydrogen- and argon-plasma treatment

The plasma-treatment experiments are performed in capacitively coupled 60-Mhz VHF discharges in a parallel-plate configuration, as shown in Fig. 4 [57,58]. The sample is placed on the electrically grounded electrode, and heated at a temperature T in the range from 120 to 240 °C. Either H_2 gas or Ar gas is introduced into a vacuum chamber from the powered electrode showerhead. The gas pressure is set at 0.3 Torr by regulating a gas flow rate of 50 sccm. The discharge is maintained by supplying a VHF discharge power P_{VHF} ranging from 3 W (23 mW/cm^2) to 50 W (390 mW/cm^2). Correspondingly, the peak-to-peak voltage V_{pp} is varied from 35 to 184 V, as measured with a high-voltage probe. The discharge period Δt (i.e., the plasma-treatment time) is set between 2.0 and 1000 s. The electrode diameter and discharge gap are 128 and 22 mm, respectively. With regard to the discharge gas (i.e., either H_2 or Ar), Δt, P_{VHF}, and T are varied. The details of the discharge conditions are given in Table I.

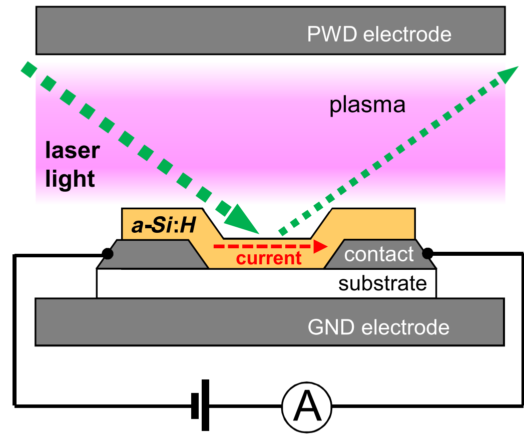

FIG. 4. Experimental setup. The sample is placed on the electrically grounded (GND) electrode. The photocurrent in a-Si:H film is measured under laser light. The intensity of laser light is modulated, and the corresponding oscillating photocurrent signal is detected by use of a lock-in technique. A plasma is generated by capacitively coupled 60-MHz discharge in a parallel-plate configuration. PWD, powered.

The discharge plasmas are characterized with a Langmuir probe [64], by energy-filtered mass spectrometry (MS), by vacuum-ultraviolet absorption spectroscopy [65], and by optical emission spectroscopy. The electron temperature is measured to be approximately 2.5 eV for H_2 plasmas at $P_{\mathrm{VHF}} = 50$ W. The ion species are measured by MS, and the dominant species is determined to be H_3^+ in H_2 plasmas [57]. From the ion saturation currents, the density of H_3^+ ions is estimated to be approximately 5×10^9 cm^{-3} at $P_{\mathrm{VHF}} = 50$ W. The ion energy distribution is single peaked, measured by energy-filtered MS. The mean ion energy, E_i, over the electrically grounded electrode increases with V_{pp}; E_i is varied from approximately 10 eV to approximately 35 eV in our H_2 discharge [57]. For the radical species, the H-atom density is determined from vacuum-ultraviolet absorption spectroscopy; $n_{\mathrm{H}} \approx 10^{12}$ cm^{-3} [66]. The energy distribution of the photons from plasmas is monitored by optical emission spectroscopy. The emission spectra of H_2 and Ar plasma at $P_{\mathrm{VHF}} = 5$ W are shown in Fig. 5. A H_2 plasma emits a large amount of UV and VUV photons in the range $\lambda \approx 200$–380 nm compared with an Ar plasma. This large amount of UV and VUV photons in a H_2 plasma originates from the dissociative emission of H_2 excited states, $a^3\Sigma_g^+ \Rightarrow b^3\Sigma_u^+$ [67,68].

C. Photocurrent measurement

The photocurrent in a a-Si:H film is measured during the plasma treatment, and also after the treatment (i.e, the postannealing) [48,49]. A a-Si:H film is illuminated with a 520-nm-wavelength laser operated at 1 mW. The photon energy of the laser light $h\nu$ is 2.38 eV, which is larger than

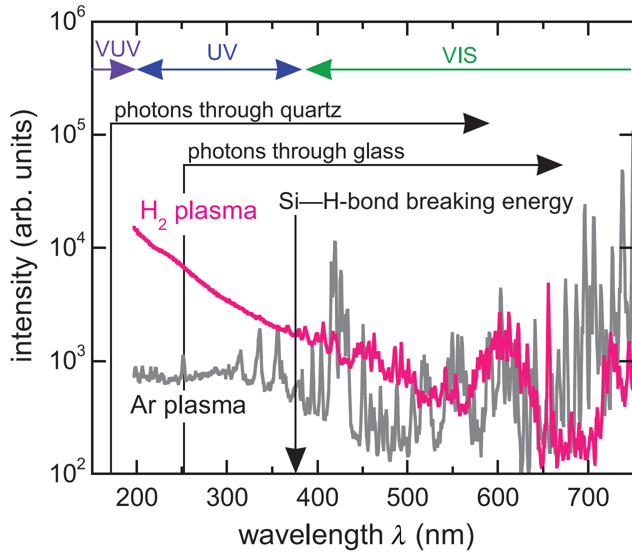

FIG. 5. Optical emission spectra for hydrogen (H_2) and argon (Ar) plasmas in the range from 200 to 750 nm. H_2 and Ar plasmas are both generated at a discharge power of 5 W. A H_2 plasma emits more UV and VUV photons compared with an Ar plasma. The Si—H-bond-breaking energy is denoted by a vertical arrow. The photons transmitted through glass and quartz are indicated by horizontal arrows.

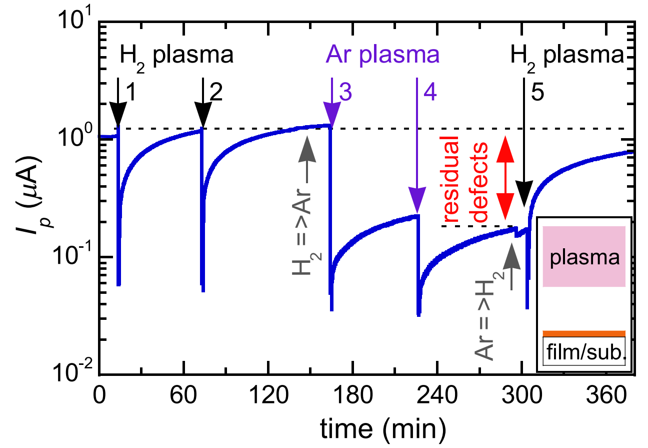

FIG. 6. Time evolution of photocurrent in *a*-Si:H film for sample A during plasma and postannealing treatments. Each plasma treatment causes a strong reduction in the photocurrent, I_p, reflecting the generation of plasma-induced defects. After the plasma treatment (i.e., during postannealing), I_p begins to increase, indicating defect recovery. I_p returns completely to the initial level for H_2-plasma treatment. In contrast, the recovery is limited in the case of Ar-plasma treatment, indicating the creation of the residual defects. The residual defects are mostly annihilated by an additional H_2-plasma and postannealing treatment, indicated by the recovery of I_p denoted by arrow 5. The discharge gas is replaced according to the aim of the treatment, which causes a small fluctuation in I_p, indicated by arrows.

the band gap E_g of 1.70 eV described above. The spot size of the laser is set to cover all of the photocurrent channels formed by the interdigitated contacts. The photogenerated carriers are collected by the interdigitated contacts, which are biased at 10 V (dc) with respect to each other. The electrons are mainly collected by the contacts since the mobility of electrons is much larger than that of holes. The intensity of the laser light is modulated to 1.111 kHz, and the photocurrent signal oscillating at this frequency is extracted by a lock-in technique. The lock-in time constant is set at 100 ms. The photocurrent signal is digitized and recorded at a rate of 2.0 Hz with an acquisition unit. By use of this lock-in technique, the laser-induced photocurrent could be distinguished from plasma-generated currents such as plasma-emission-induced photocurrent and ion current.

IV. RESULTS

In this section, we show the time evolution of the photocurrents in *a*-Si:H films during the plasma treatment and postannealing. The results are shown for samples A, B, C, and D to distinguish the effects of ion bombardment, radical exposure, and photon irradiation on the generation of defects.

A. Plasma-induced defects

Figure 6 shows the time evolution of the photocurrent, I_p, in a *a*-Si:H film for sample A during plasma treatment and postannealing. The following treatments are performed: H_2-plasma treatment twice (denoted by arrows 1 and 2), followed by Ar-plasma treatment twice (denoted by arrows 3 and 4), and H_2-plasma treatment again (indicated by arrow 5). The conditions of these plasma treatments are $\Delta t = 1$ min, $P_{\mathrm{VHF}} = 5$ W, and $T = 200\,^{\circ}$C. During these plasma treatments, the film etch is small; it is approximately 1 nm for H_2-plasma treatment and it is below the detection limit for Ar-plasma treatment. The interval between each treatment (i.e., the postannealing period) is roughly 70 min. The film is thus annealed until the next treatment. The discharge gas is replaced according to the aim of the treatment, denoted by $H_2 \Rightarrow$ Ar or Ar $\Rightarrow H_2$.

We find that each H_2- and Ar-plasma treatment causes a strong reduction in I_p, typically by 1 order of magnitude. The reduction in I_p begins immediately after initiation of the discharge/treatment; the decay time of I_p is less than 100 ms, which is limited by the lock-in time constant (Sec. IIIC). The observed strong reduction indicates the generation of defects (i.e., plasma-induced defects). Since $I_p \propto 1/n_d$ in Eq. (1), the defect density is expected to increase by 1 order of magnitude during the plasma treatment.

Once the discharge/treatment has been terminated, I_p begins to increase with time, showing a defect-recovery trend. This recovery behavior of I_p is different depending

on whether H_2- or Ar-plasma treatment was performed before. For H_2-plasma treatment, I_p returns completely to the initial level (approximately 1.2 μA) after annealing. In contrast, it does not return to the initial level for Ar-plasma treatment; I_p returns to only approximately 20% (approximately 0.25 μA) of the initial level. The results suggest that the H_2-plasma-induced defects are annihilated completely by annealing, whereas the Ar-plasma-induced defects are not, and some of these defects remain in the film. However, these remaining defects, (i.e., the residual defects) are mostly annihilated by an additional H_2-plasma treatment (denoted by arrow 5) and postannealing. This suggests that H_2-plasma treatment is beneficial for the annihilation of Ar-plasma-induced residual defects.

From the time evolution of I_p during the postannealing, the characteristic time for the defect annihilation can be estimated; it is several tens of minutes at a annealing temperature T of 200 °C. This characteristic time is strongly dependent on T. Later, we show a relation between the characteristic time and the annealing temperature, yielding an Arrhenius plot, to discuss the activation energy for the defect annihilation (see Sec. IV E).

B. Radical- and photon-induced defects

The radical- and photon-induced defects are recognized from the results of H_2- and Ar-plasma treatment for sample B, as shown in Fig. 7. Each treatment causes a strong reduction in I_p, similar to that observed in the case of sample A, indicating defect generation due to radical exposure and photon irradiation. However, these defects are mostly annihilated by annealing, indicated by the recovery of I_p to nearly the initial level. This recovery behavior of I_p is different from that observed for sample A with Ar-plasma treatment (compare I_p denoted by arrows 3 and 4 in Figs. 6 and 7). Therefore, we can conclude that the residual defects are created by Ar^+-ion bombardment rather than radical exposure and photon irradiation.

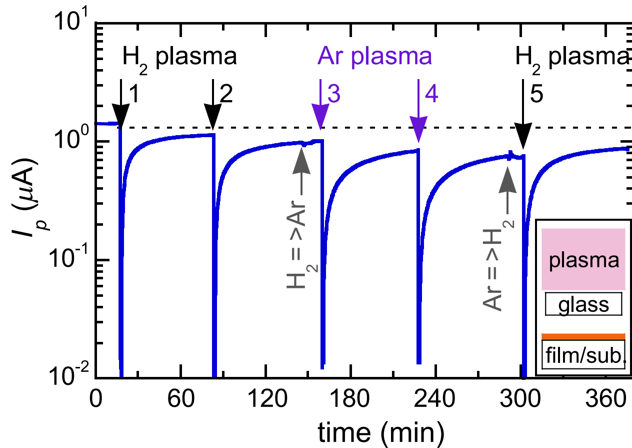

FIG. 7. Time evolution of I_p in a-Si:H film for sample B during radical and photon exposure, and consecutive postannealing. Each exposure of H_2- and Ar-related radicals and photons causes a strong reduction in I_p, reflecting the generation of radical- and photon-induced defects. These defects are annihilated by the postannealing, indicated by the recovery of I_p to the initial level.

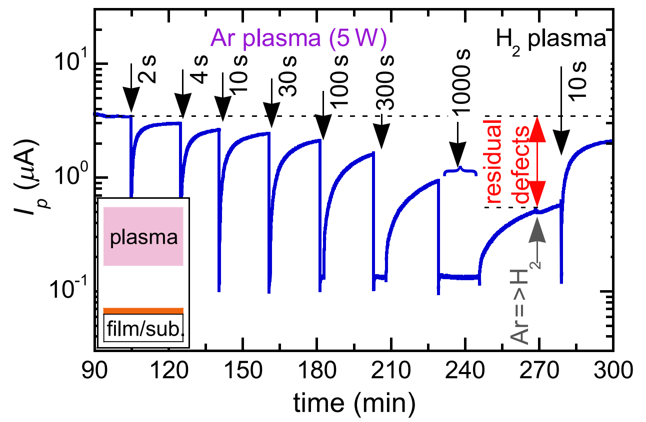

FIG. 8. Time evolution of I_p in a-Si:H film for sample A during Ar-plasma and postannealing treatments. The treatment time is varied from 2 to 1000 s. The recovery level of I_p at the end of postannealing is lowered by increase of the treatment time, indicating the creation of more residual defects.

C. Ar^+-ion-bombardment-created residual defects

To study the creation of the residual defects, we perform Ar-plasma treatment of sample A under various conditions. Figures 8 and 9 show the time evolution of I_p for different Δt and P_{VHF}, respectively. As shown in Fig. 8, increase of Δt from 2 to 1000 s results in the creation of more residual defects, indicated by a larger reduction of I_p at the end of the annealing. On the other hand, the amount

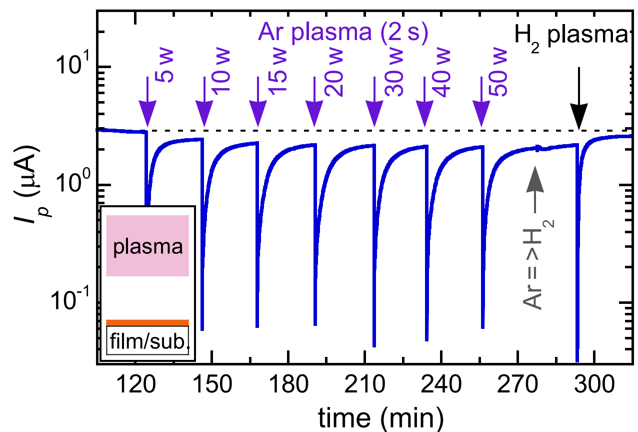

FIG. 9. Time evolution of I_p in a-Si:H film for sample A during Ar-plasma and postannealing treatments. The discharge power is varied from 5 to 50 W. The recovery level of I_p at the end of postannealing is roughly the same, and is not strongly dependent on the discharge power.

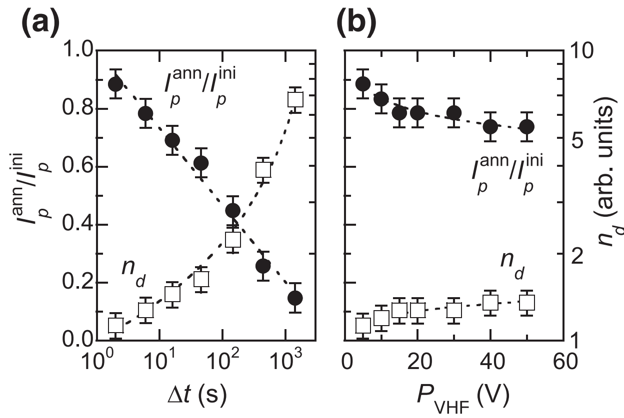

FIG. 10. Photocurrent reduction and relative density of residual defects. The photocurrent at the end of postannealing is normalized by the initial level, I_p^{ann}/I_p^{ini}. The relative density of the Ar-plasma-induced residual defects is calculated by $n_d \propto (I_p^{ann}/I_p^{ini})^{-1}$. (a) I_p^{ann}/I_p^{ini} decreases logarithmically with the Ar-plasma-treatment time, Δt. Correspondingly, n_d strongly increases with Δt. (b) I_p^{ann}/I_p^{ini} decreases slightly with the discharge power, P_{VHF}, and n_d slightly increases.

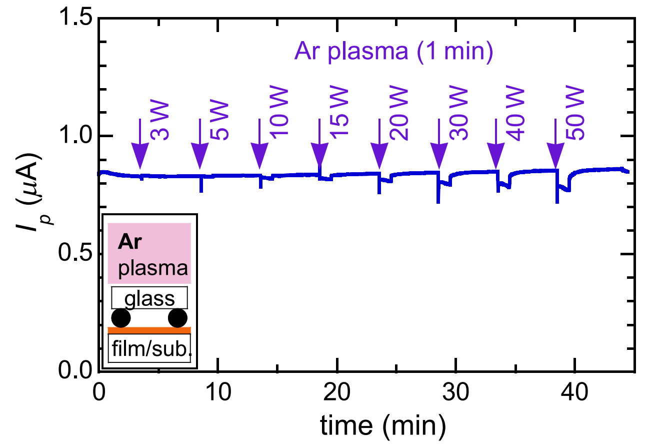

FIG. 11. Time evolution of I_p in *a*-Si:H film for sample C during irradiation with visible photons emitted from Ar plasma and postannealing. During photon irradiation, I_p is slightly reduced. After photon irradiation, I_p returns completely to the initial level.

of the residual defects is not increased even though P_{VHF} is increased significantly, as shown in Fig. 9.

To quantitatively characterize the creation of the residual defects, we introduce a dimensionless parameter of the photocurrent, I_p^{ann}/I_p^{ini}, where I_p^{ini} is the photocurrent in the initial state (i.e., before any Ar-plasma treatments) and I_p^{ann} is the photocurrent at the end of the annealing. With I_p^{ann}/I_p^{ini}, we can examine the relative change of the density of the residual defects, by $n_d \propto (I_p^{ann}/I_p^{ini})^{-1}$. Figure 10 shows I_p^{ann}/I_p^{ini} and n_d as a function of Δt and P_{VHF}, obtained from the data in Figs. 8 and 9. As in Fig. 10(a), I_p^{ann}/I_p^{ini} decreases logarithmically with Δt, and thus n_d is increased significantly. For example, n_d is increased by approximately 7 times compared with the initial state (i.e., before any plasma treatments). On the other hand, I_p^{ann}/I_p^{ini} and n_d do not show strong changes even though a large P_{VHF} is applied [Fig. 10(b)]. For example, I_p^{ann}/I_p^{ini} decreases by approximately 25% for a treatment at $P_{VHF} = 50$ W, and n_d increases by approximately 33%. Both I_p^{ann}/I_p^{ini} and n_d exhibit tendencies to be saturated for higher P_{VHF} (i.e., V_{pp}). These results suggest that the continuous bombardment of Ar^+ ions is more effective in creating the residual defects than a strong impact and/or a large flux of Ar^+ ions in a short period.

D. Photon-induced defects

The photon-induced defects are studied with samples C and D. As shown in Fig. 5, the H_2 plasma emits more UV photons than the Ar plasma; therefore, the UV-photon-induced defects can be examined by comparing I_p in sample C for these two types of plasma emission. Besides, the effects of VUV photons can be distinguished via a reduction in I_p of sample D with quartz glass because it transmits VUV photons with energy up to approximately 7.9 eV.

The results for I_p for photon irradiation/treatment with an Ar plasma at various P_{VHF} are shown in Fig. 11. During photon irradiation, I_p is reduced slightly, and the reduction is enhanced by increase of P_{VHF}. The reduced I_p is, however, returned to the initial level after the irradiation. This recovery of I_p occurs in a short period of approximately 1 min or less. The residual defects are not created by photon irradiation.

Figure 12 shows the results for I_p for photon irradiation by a H_2 plasma at various P_{VHF}. Apparently, the reduction

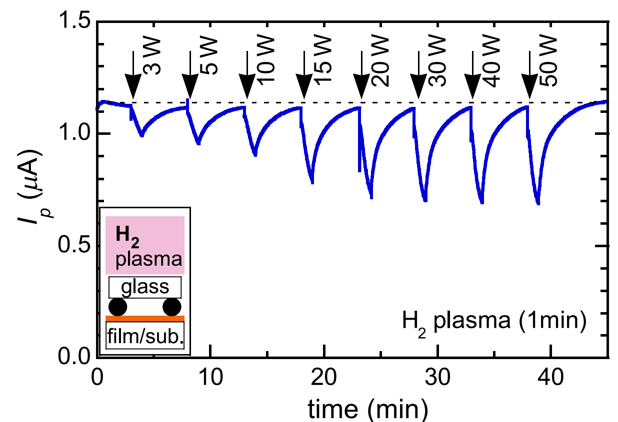

FIG. 12. Time evolution of I_p in *a*-Si:H film for sample C during irradiation with UV photons emitted from H_2 plasma and postannealing. During photon irradiation, I_p is reduced. The reduction is enhanced by increase of P_{VHF}. After photon irradiation, I_p returns completely to the initial level.

in I_p during photon irradiation by a H_2 plasma is more pronounced compared with that for an Ar plasma. Increase of $P_{\rm VHF}$ results in a greater reduction in I_p. This reduced I_p again returns to the initial level by annealing. From these two photon-irradiation experiments, we can draw brief conclusions on the photon-induced defects. Firstly, UV photons generate more defects than visible photons. Secondly, the amount of UV-photon-induced defects increases with the UV-photon flux. Thirdly, the photons do not create the residual defects; the photon-induced defects are annihilated completely by annealing.

To qualitatively examine the UV-photon-induced defects, we define a dimensionless parameter, $I_p^{\rm UV}/I_p^{\rm ini}$, similar to that used in Sec. IVC. Here $I_p^{\rm UV}$ is the photocurrent at the end of the photon-irradiation period. For this time, n_d is expressed as $n_d \propto (I_p^{\rm UV}/I_p^{\rm ini})^{-1}$. Figure 13(a) shows $I_p^{\rm UV}/I_p^{\rm ini}$ and n_d as a function of $P_{\rm VHF}$, related to the UV-photon flux. As seen, $I_p^{\rm UV}/I_p^{\rm ini}$ monotonically decreases with increasing $P_{\rm VHF}$, which yields a steady increase in n_d. In the present experiments, n_d increases by 70% at $P_{\rm VHF}$ = 50 W with respect to the initial state without any irradiation.

The annealing effects on the photon-induced defects are studied with sample C. The time evolution of I_p at various T is shown in Fig. 14. As clearly seen, I_p decreases more for lower T by photon irradiation, and takes longer to return to the initial level by annealing. The reduction in I_p and the relative change of the defect density are plotted in Fig. 13(b). At low T of 120 °C, I_p is reduced to approximately 20% of the initial level and n_d is increased by a factor of approximately 5. On the other hand, at high T of 240 °C, I_p is slightly reduced and n_d is not substantially increased.

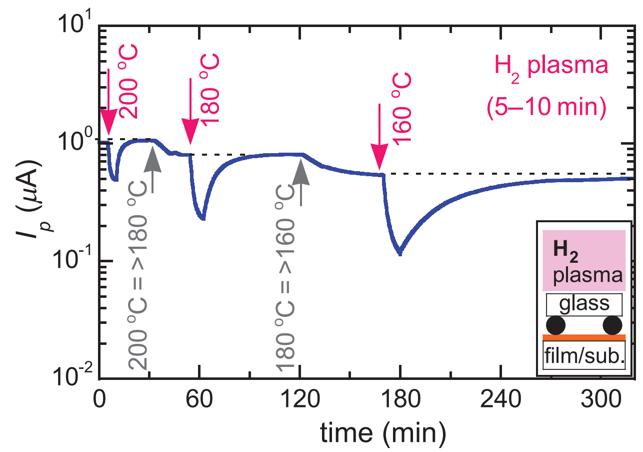

FIG. 14. Time evolution of I_p in a-Si:H film for sample C during irradiation with UV photons emitted by H_2 plasma and postannealing. The irradiation and annealing are performed at 200, 180, and 160 °C. Irradiation at a lower temperature causes a larger reduction in I_p. The recovery of I_p takes longer for a lower annealing temperature.

In addition, the effects of VUV photons are studied with sample D. The time evolution of I_p is shown in Fig. 15. By comparing the data at 180 °C in Figs. 14 and 15, we note that I_p is more rapidly and strongly reduced by VUV-photon irradiation and takes longer to return to the initial level by annealing. The reduction in I_p caused by the VUV photons and the corresponding increase in n_d are plotted as symbols with arrows in Fig. 13(b). It is clearly seen

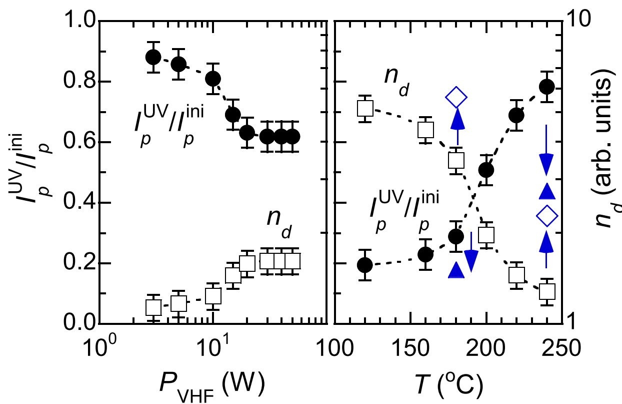

FIG. 13. Photocurrent reduction and UV-photon-induced defects. The photocurrent reduction at the end of the photon-irradiation period is normalized by the initial level, $I_p^{\rm UV}/I_p^{\rm ini}$. The relative density of the photon-induced defects is given by $n_d \propto (I_p^{\rm UV}/I_p^{\rm ini})^{-1}$. (a) $I_p^{\rm UV}/I_p^{\rm ini}$ decreases with increasing $P_{\rm VHF}$, which yields an increase in n_d. (b) $I_p^{\rm UV}/I_p^{\rm ini}$ increases with annealing temperature, T. Correspondingly, n_d decreases with T. For the effects of VUV photons, the data are shown by triangles and diamonds with arrows.

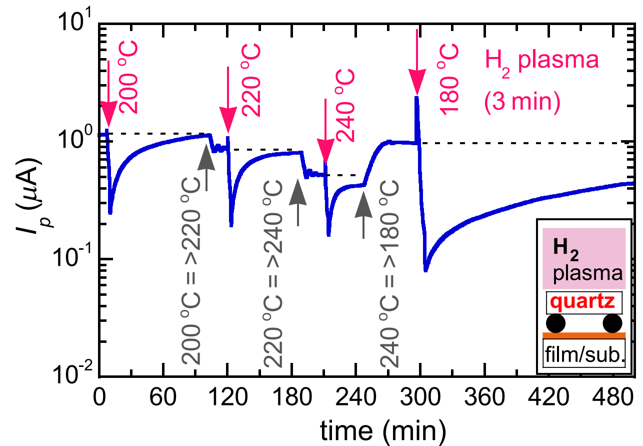

FIG. 15. Time evolution of I_p in a-Si:H film for sample D during irradiation with VUV photons emitted by H_2 plasma and postannealing. The irradiation and annealing are performed at 200, 220, 24,0 and 180 °C. The VUV photon irradiation causes a larger reduction in I_p. The recovery of I_p takes longer for a lower annealing temparature.

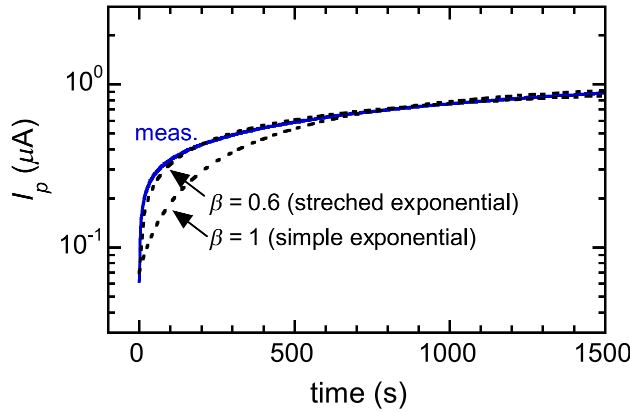

FIG. 16. Time evolution of I_p in *a*-Si:H film for sample A after H_2-plasma treatment (i.e., during postannealing). The data are obtained at $T = 200\,°\mathrm{C}$ and $P_{\mathrm{VHF}} = 5$ W. The experimental data are denoted by a solid line. Fits with simple exponential and stretched exponential functions are shown by broken lines. A stretched exponential function yields a better fit than a simple exponential one. The best fit yields a characteristic time of $\tau = 808$ s and a dispersion factor of $\beta = 0.6$. With this τ obtained at various temperatures, an Arrhenius plot is prepared, shown in Fig. 17.

that irradiation by VUV photons at lower T generates more defects.

E. Defect annihilation and activation energy

Defect annihilation, monitored by the recovery of I_p, takes a finite time. According to the experiments, the recovery time of I_p depends on two factors: the annealing temperature and the origin of the defect generation (i.e., ions, radicals, photons, and their mixture, i.e., a plasma). Here we analyze the time evolution of I_p during postannealing by using a stretched exponential term that takes into account the dispersive nature of amorphous materials [69–71]:

$$I_p(t) = I_{p0}(1 - \exp\{-[(t - t_{\mathrm{off}})/\tau)]^{\beta}\}) + I_p(t_{\mathrm{off}}), \quad (2)$$

where I_{p0} and β are the preexponential factor and the stretch parameter, respectively, τ is the recovery time of I_p (i.e., the characteristic time for defect annihilation), and t_{off} denotes the time at the end of the treatment.

An example of a fit by the stretched exponential term is shown in Fig. 16. The data are obtained from sample A after H_2-plasma treatment at 200 °C. The fit gives $\tau = 808$ s and $\beta = 0.6$. For comparison, a simple exponential ($\beta = 1$) is also shown in Fig. 16. One can see that the stretched exponential term yields a better fit than a simple exponential. From the fit with Eq. (2), we determine τ at various T for samples A, B, C and D to make an Arrhenius plot.

Figure 17 shows $1/\tau$ versus $1000/T$ (i.e., an Arrhenius plot for defects generated by various treatments).

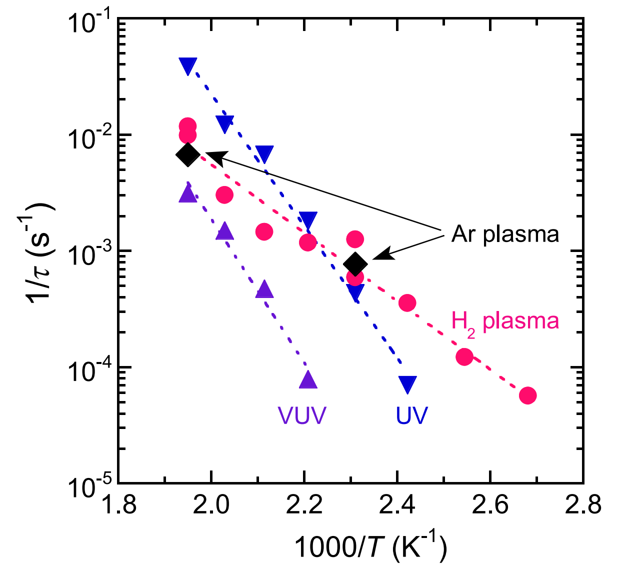

FIG. 17. Arrhenius plot ($1/\tau$ vs $1000/T$) for defect annihilation. The experimental data for $1/\tau$ show an exponential decay with $1000/T$, indicating that defects are annihilated due to thermal activation processes. The data for H_2- and Ar-plasma-induced defects are denoted by circles and diamonds, respectively. Some data for H_2-plasma-induced defects are replotted from Ref. [48]. The data for UV- and VUV-photon-induced defects are denoted by inverted and upright triangles, respectively. The slope of $1/\tau$, related to the activation energy, E_a, is different depending on the origin of defect generation. The activation energy E_a for plasma-induced defects is 0.53 ± 0.06 eV, which is smaller than the activation energy for the photon-induced defects, 1.17 ± 0.06 eV, denoted by dotted lines. The preexponential factor, k_0, is different between the UV- and VUV photon-induced defects: it is larger for UV-photon-induced defects.

The following results are found. Firstly, $1/\tau$ shows a exponential decay with $1/T$, indicating that a thermal activation process plays an important role in defect annihilation. Secondly, the exponentially decaying slope is different between the photon-induced and the plasma-induced defects; it is steeper for the photon-induced defects. To obtain the activation energy, E_a, the slope is fitted by

$$1/\tau = k_0 \exp(-E_a/k_B T), \quad (3)$$

where k_0 and k_B are the preexponential factor and the Boltzmann constant, respectively. We find $E_a = 0.53 \pm 0.06$ eV for the plasma-induced defects and $E_a = 1.17 \pm 0.06$ eV for the photon-induced defects in the range $T = 120$–$240\,°\mathrm{C}$. In this temperature range, τ varies in a wide range from approximately 25 s at $T = 240\,°\mathrm{C}$ to approximately 20 000 s at 120 °C. Thirdly, the values of τ are roughly the same between H_2- and Ar-plasma-induced defects at a given T although Ar-plasma treatment causes the residual defects and H_2-plasma treatment does not. Fourthly, k_0 is different between the UV- and

VUV-photon-induced defects, while the activation energies are nearly the same between them; k_0 is smaller for the VUV-photon-induced defects. It takes longer to anneal the sample, as described in Sec. IVD. This point is discussed in Sec. V G.

V. DISCUSSION

Here we discuss the defect kinetics with plasma treatment and postannealing. To do that, we briefly describe the length of penetration of photons, radicals, and ions into the film. We introduce a defect-rich surface layer, and explain a rate equation for the generation and annihilation of defects. In the rate equation, each term is examined according to the experimental observations. The dominant species for the generation of defects during the plasma treatment are discussed. For the annihilation of defects, the activation energy is discussed in terms of microstructural disordering. Finally, a possible mechanism for the creation of residual defects and the annihilation of those defects by H_2-plasma treatment are described from the viewpoint of hydrogen kinetics.

A. Penetration length, defect-rich surface layer, and carrier diffusion

During plasma treatment, photons, radicals, and ions penetrate into a *a*-Si:H film, where they can generate defects such as DBs. The penetration lengths of these species are different depending on their energy and reactivity. For example, UV photons penetrate into the film on a scale of several tens of nanometers, l^{UV} [18,19]. For metastable Ar atoms (Ar*) [72], the penetration is limited since their internal energy is efficiently transferred to the surface atoms. So, the penetration length, l^{Ar^*}, is supposed to be on the order of subnanometers. In contrast, the H atoms penetrate deeply into the film by diffusion; the penetration length, l^{H}, is a few tens of nanometers [31,32,73,74]. For Ar^+ ions, the penetration length, l^{Ar^+}, is a few nanometers at an incident energy of a few tens of electronvolts [12,13].

The generation of defects is thus localized near the surface, since the penetration lengths, descried above, are less than the film thickness ($d > l^{\mathrm{UV}} \gtrsim l^{\mathrm{H}} > l^{\mathrm{Ar}^+} > l^{\mathrm{Ar}^*}$). The generated defects are highly limited to diffuse under the conditions of low-temperature experiments, and therefore we can consider the formation of a defect-rich surface layer [11,27,75–77], as shown in Fig. 1. In this layer, the defects are distributed in the direction perpendicular to the film surface; the density of defects decreases with the distance from the surface. The thickness of the defect-rich surface layer, d_s, may change depending on the origin of the defect generation. For instance, d_s is supposed to be approximately l^{H} for H_2-plasma treatment and approximately l^{Ar^*} for Ar-plasma treatment. Here we assume that the radicals are the dominant species for the generation of defects. This is confirmed by the experimental results shown in Figs. 6 and 7, and is discussed in Sec. VD.

According to the spatial distribution of defects, the photocurrent in the film could be distributed vertically as well. Nevertheless, a change of the photocurrent measured in the experiments primarily reflects the generation/annihilation of defects in the defect-rich surface layer. This is because the density of defects in this surface layer is significantly higher than that in the bulk, as indicated in Sec IV A. Besides, the diffusion of carriers (electrons) from the bulk to the defect-rich surface layer strongly enhances the recombination, as denoted by a zigzag line in the middle left of Fig. 1. The diffusion length of electrons in a *a*-Si:H film is typically several tens of nanometers [78], which is not small enough compared with the thickness of the *a*-Si:H film used in this study. Therefore, the photocurrent is restricted mainly by the defects in the defect-rich surface layer.

B. Rate equation for generation and annihilation of defects

The defect kinetics in the defect-rich surface layer can be described by a rate equation. In general, the defects are generated and/or annihilated by photon irradiation, radical exposure, ion bombardment, and thermal effects. Taking these effects into account, we can express the rate of change of the defect density as follows:

$$\begin{aligned}\frac{\partial n_d}{\partial t} &= \nu_g^p(n_M - n_d) - \nu_a^p n_d + \nu_g^r(n_M - n_d) - \nu_a^r n_d \\ &\quad + \nu_g^i(n_M - n_d) - \nu_a^i n_d + \nu_g^T(n_M - n_d) - \nu_a^T n_d \\ &\quad + D\frac{\partial^2 n_d}{\partial^2 z},\end{aligned} \tag{4}$$

where ν_g^p, ν_g^r, ν_g^i, and ν_g^T are the rates of generation of defects by photons, radicals, ions, and thermal effects, respectively; n_M is the maximum value of the density of possible defects, corresponding to the existence of the maximum density of weak bonds that can be broken by the reactions with those species; ν_a^p, ν_a^r, ν_a^i, and ν_a^T are the rates of annihilation of defects by photons, radicals, ions, and thermal effects, respectively; and the last term expresses the diffusion of defects, which can be driven thermally. The last term is ignored because D is small for DBs in *a*-Si:H at low temperature [32]. Instead, the diffusion of mobile hydrogen may play an important role in the generation and annihilation of defects particularly for *a*-Si:H [32]. These effects can be included in the third and fourth terms, respectively.

In the experiments, the annihilation of defects associated with photon irradiation and ion bombardment is not observed. In addition, the generation of defects associated with thermal effects is not observed since the experiments

are performed at a relatively low temperature of 240 °C or less. Thus, Eq. (4) can be simplified as follows:

$$\frac{\partial n_d}{\partial t} = \nu_g^p(n_M - n_d) + \nu_g^r(n_M - n_d) - \nu_a^r n_d + \nu_g^i(n_M - n_d) - \nu_a^T n_d. \quad (5)$$

The solution of this equation is well known. It is a simple exponential form.

To include the dispersive nature of *a*-Si:H, which is observed in many experiments [69], Eq. (5) can be extended in the simplest manner by our assuming that all of the terms have the same dispersive properties [69], leading to

$$\frac{\partial n_d}{\partial t} = \left(\frac{t}{P}\right)^{\beta-1} \left[\nu_g^p(n_M - n_d) + \nu_g^r(n_M - n_d) - \nu_a^r n_d + \nu_g^i(n_M - n_d) - \nu_a^T n_d\right], \quad (6)$$

where β is the stretch parameter, related to the breadth of the distribution of contributing processes ($\beta < 1$), and P is a scaling factor that preserves the dimensions. This equation is phenomenological, but yields a solution in a stretched exponential function:

$$n_d(t) = n_{\text{sat}} - (n_{\text{sat}} - n_0)\exp\left[-(t/\tau)^\beta\right], \quad (7)$$

where n_{sat} is the density of defects in the steady state ($t \to \infty$) and n_0 is the initial density. This equation describes both generation and annihilation depending on whether $n_{\text{sat}} > n_0$ or not. The plasma-treatment experiments correspond to $n_{\text{sat}} > n_0$, whereas the postannealing experiments correspond to $n_{\text{sat}} < n_0$. In the results of the annealing experiment shown in Fig. 16, the time evolutions of I_p are well fitted with the stretched exponential form rather than a simple exponential ($\beta = 1$). This means that the annihilation of defects is governed by the dispersive nature. The origins of the dispersive nature are discussed in earlier studies [69]. It is widely known that the structural disorder of amorphous materials accounts for this nature. Such structural disorder may be induced by the spatial distribution of defects generated by plasma processing. In the following sections, the generation of defects is discussed in terms of photon irradiation, radical exposure, ion bombardment, and plasma treatment.

C. Photon-induced defects

UV-photon-induced defects are clearly observed in the experiments with samples C and D. The generation of these defects depends on two parameters: the UV-photon flux and energy. As shown in Fig. 13(a), n_d increases with increasing photon flux (i.e., P_{VHF}). The formation of these defects is saturated at a high-flux condition of $P_{\text{VHF}} \gtrsim 30$ W, indicating the existence of n_M in Eq. (6) for the UV-photon-induced defects [55,79,80]. In this study, n_M is expected to be roughly 70% more than n_d in the initial state. This value is relatively small compared with the values of samples that experienced light-induced degradation under standard conditions (AM1.5, 1SUN, and 25 °C) of illumination for solar cells [55,79,80]. In the experiments, the photon irradiation is performed at $T = 200$ °C, which is higher than that of standard conditions at 25 °C. In such a case, the thermal-annealing effect plays an important role in the annihilation of defects during photon irradiation, and thus n_M is limited to a relatively small number. For the influence of VUV photons, the data are shown as triangles and diamonds with arrows in Fig. 13(b). Apparently, the VUV photons generate more defects, indicating that stronger Si—H and/or Si—Si bonds are broken. These photon-induced defects are, however, annihilated completely by the annealing [81].

As shown in Fig. 13(b), the annealing effects are observed even in the photon-irradiation period. Increase of the processing temperature results in the formation of fewer defects. A high annealing temperature of 240 °C strongly suppresses the UV-photon-induced defects, which indicates rapid and effective annealing of defects.

D. Radical-induced defects

Radical-induced defects are confirmed by a strong reduction in I_p, denoted by arrows 1–5 in Fig. 7. In our experiments, the dominant radical species are H atoms for H_2 plasmas and Ar* atoms for Ar plasmas. The H-atom density is on the order of 10^{12} cm^{-3} [66], as described in Sec. III B. The Ar* atoms possess two metastable states at the $(3p^5 4s)^3P_2$ level and the $(3p^5 4s)^3P_0$ level, which are located 11.55 and 11.72 eV above the ground state, respectively [72]. The density of Ar* is estimated by our performing fluid simulations of Ar discharge in our experimental conditions; it is on the order of 10^{11} cm^{-3}. The generation of defects by these radicals is highly pronounced compared with that by UV photons (see the reduction in I_p between Figs. 7 and 12), indicating $\nu_g^r \gg \nu_g^p$ in the rate equation in Eq. (6). The amount of defects generated by the radicals is expected to be 1 or 2 orders of magnitude higher than that of the initial state. Comparing the amount of defects generated by H and Ar* radicals, we note that they are roughly the same. This is indicated by roughly the same amount of reduction in I_p denoted by arrows 3 and 5 in Fig. 7. These radical-induced defects are almost recovered by postannealing, similarly to the photon-induced defects.

We now describe a possible mechanism for the generation and annihilation of radical-induced defects (see Fig. 18). Firstly, we consider the generation of defects by Ar* radicals. During radical exposure, Ar* radicals diffuse toward the film surface and their internal energies are transferred to the surface Si—H bonds. The internal energy

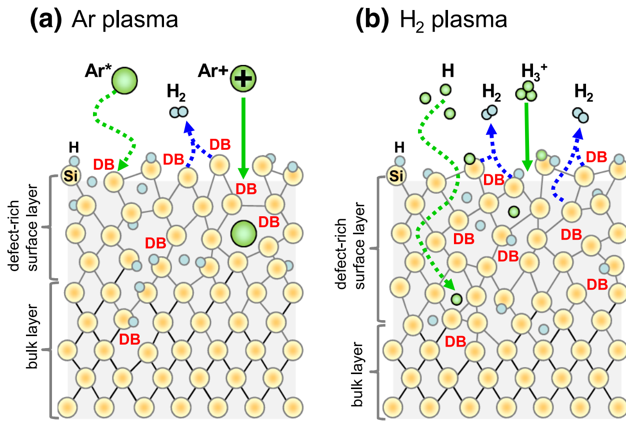

FIG. 18. Microstructure and defects in *a*-Si:H during plasma treatment. (a) During Ar-plasma treatment, the defects are generated mainly by metastable Ar atoms (Ar*). The internal energy of Ar* is transferred to the surface atoms, resulting in Si—H and Si—Si bond breaking (i.e., the generation of DBs). The bombardment of Ar^+ ions may cause local heating, which induces the desorption of H atoms as H_2 molecules. Thus, a H-atom-deficient state is formed in the defect-rich surface layer. This is a possible reason for the creation of the residual defects. In addition, the residual defects are created by the penetration of Ar^+ ions. These Ar^+ ions are neutralized and stay in the film. They behave as impurities. (b) During H_2-plasma treatment, the defects are generated mainly by H atoms. The H atoms diffuse into the film, where they react with weak bonds, resulting in bond breaking (i.e., the generation of DBs). The density of DB defects is high and the microstructure is highly disordered in the defect-rich surface layer. The excess H atoms, supplied by a H_2 plasma, are mobile, denoted by a zigzag line in the upper left.

of Ar* radicals, described above, is large enough to break the Si—H bonds, with a binding energy of approximately 3.6 eV [82], and the Si—Si bonds, with a binding energy of 4.64 eV. The broken bonds (i.e., DBs) are expected to stay near the surface, and the mobile H atoms released from the Si—H bonds also stay mostly near the surface (see the upper left of Fig. 18(a)), forming the defect-rich surface layer. These mobile H atoms are supposed not to be desorbed as H_2 molecules from the surface. After the exposure (i.e, during the postannealing), the DBs in the defect-rich surface layer are terminated by H atoms located around them. Because the mobile H atoms are not desorbed and Ar* radicals do not penetrate into the film, the DB defects are terminated by H atoms, forming a network structure similar to the initial state before the exposure. Thus, the Ar*-radical-induced defects are recovered by the postannealing, and the Ar* radicals do not create the residual defects.

On the other hand, a possible mechanism for the generation and annihilation of H-radical-induced defects is different from that mentioned above. During radical exposure, the H atoms penetrate deeply into the film by diffusion, and they react with the weak bonds of Si—H and Si—Si in a network structure, as in Fig. 18(b). The reactions cause bond breaking (i.e., the formation of DBs). The DBs and excess (mobile) H atoms supplied from the plasma are distributed in the depth of l^H from the surface, which forms the defect-rich surface layer. After exposure, the excess H atoms are considered to diffuse out from the surface, which induces the reorganization of the defect-rich surface layer, associated with the termination of DBs by H atoms. This kind of reorganization process, including the termination of DBs, is described in early studies [31,32].

E. Dominant species for defect generation

During the plasma treatments, the generation of defects by ion bombardment is not clearly distinguished from that by radical exposure. Comparing the reductions in I_p for samples A and B during the plasma treatments in Figs. 6 and 7, we note that the levels of reduction of I_p are roughly the same. This means that during the plasma treatments, the defects are generated dominantly by radical exposure rather than ion bombardment; that is, $\nu_g^r \gg \nu_g^i$ in Eq. (6). The dominant species responsible for the generation of defects are thus radicals such as H and Ar*. The reason for this is primarily a large difference between the densities of ions and radicals. The densities of radicals are higher than those of ions by 2–3 orders of magnitude. As described in Secs. III B and VD, the densities of H and Ar* radicals are on the order of 10^{11}–10^{12} cm^{-3}, whereas the densities of H_3^+ and Ar^+ are on the order of 10^9 cm^{-3} [57]. Another reason is the energy of ion bombardment. The energy of ions incident on the film is a few tens of electronvolts in this study, as described in Sec III B, so the generation of multiple (cascade) defects does not occur. This kind of defect-generation process is important for plasma etching/implantation processes where the incident ions are accelerated at a few hundred/thousand electronvolts in the plasma sheath [12–15].

F. Ar^+-ion-created residual defects and H-atom-mediated defect annihilation

Although ions are not dominant species for the generation of defects, the bombardment effects of Ar^+ ions are clearly observed as the creation of the residual defects, denoted by arrows 3 and 4 in Fig. 6. The amount of residual defects increased with the treatment time (Fig. 8) rather than the discharge power (Fig. 9). The creation of residual defects does not strongly depend on the incident energy and/or flux of Ar^+ ions. A possible explanation for this is the desorption of H atoms as H_2 molecules from the surface, leaving the DBs, shown in the upper middle part of Fig. 18(a). The desorption could be promoted by the local surface heating associated with a microstructural disordering. A prolonged treatment may result in more heating, which results in microstructural disordering with lots of broken bonds and H atoms. The desorption of H

atoms as H_2 molecules causes a H-atom-deficient state near the surface, which could be the origin of the residual defects.

However, the Ar^+-ion-created residual defects are mostly recovered by an additional H_2-plasma treatment and postannealing, as shown in Fig. 8. This can be interpreted as follows, similar to the process described for H-radical exposure (in Sec. VD). The H atoms supplied from the H_2 plasma diffuse into the film, which may cause the disordering of a network structure, having a lot of broken bonds and excess H atoms. After the H_2-plasma treatment, the excess H atoms diffuse out and the disordered structure can be reorganized by termination of the DBs with H atoms. The structure formed by this reorganization is expected to be similar to the initial structure before the Ar-plasma treatment. However, the structure is not completely recovered, because some of the Ar^+ ions penetrate into the film, and they are neutralized and stay in the film, as schematically shown in Fig. 18(a). These neutralized Ar atoms (i.e., impurities) are considered to be one of the origins of the residual defects, which cannot be completely removed by an additional H_2-plasma and annealing treatment. Another possible origin is the increased disorder caused by the presence of the Ar atoms in the network structure. The defect density is known to increase with the disorder, which can be characterized by the Urbach energy [60]. This can be seen in the data denoted by arrow 5 in Fig. 6, showing I_p not to completely return to the initial level.

G. Activation energy for defect annihilation

The defects generated by photons, radicals, and ions are recovered partially or completely by thermal annealing. Defect recovery takes a finite time, which is determined by a fit of I_p in the form of the stretched exponential in Eq. (2). The activation energy E_a is then obtained from the Arrhenius plots (i.e., $1/\tau$ vs $1000/T$) shown in Fig. 17.

We find E_a depends on the origin of the defect generation (i.e., whether the defects are generated by photons or plasma treatments including radicals and ions). As described in Sec. IV E, the plasma-induced defects exhibit $E_a = 0.53 \pm 0.06$ eV [48], which is significantly smaller than that of photon-induced defects, $E_a = 1.17 \pm 0.06$ eV. Such a small value of $E_a \sim 0.5$ eV was reported in early studies for H diffusion [30–32]. This means that the plasma-induced defects have a lower barrier to recovery (i.e., to be easily terminated by H atoms). This may imply the formation of a disordered structure in the defect-rich surface layer by the plasma treatment, as in Fig. 18. We suppose that in this disordered structure, mobile H atoms can diffuse easily through less-dense and porous regions. Because of this, the annihilation of defects occurs at lower annealing temperature, and thus E_a becomes smaller for the plasma-induced defects.

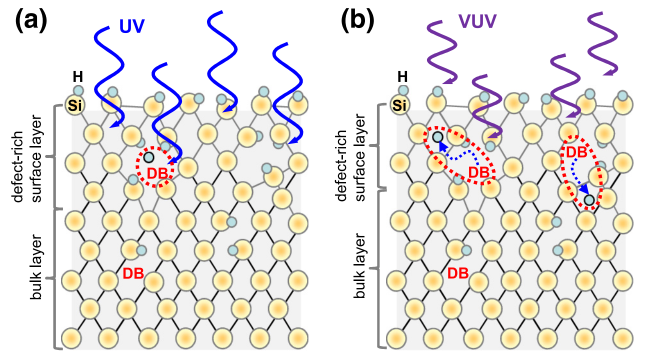

FIG. 19. Microstructure and defects in *a*-Si:H during photon irradiation. Photon irradiation causes the generation of DB defects by dissociating weak Si—H bonds. The excess energy of a mobile H atom released from a Si—H bond can be different depending on the energy of the photons. (a) In the case of UV-photon irradiation, a H atom stays near the DB. (b) In the case of VUV-photon irradiation, a H atom released from a Si—H bond travels a short distance because it has larger excess energy compared with that for UV photons. The density of DB defects is low, and thus the microstructure in the defect-rich surface layer is not strongly deformed.

On the other hand, E_a for the photon-induced defects is large. Similar values of $E_a = 0.9$–1.3 eV were reported in earlier studies [84]. Such a large value of E_a can be explained as follows. The density of defects generated by photon irradiation is smaller than that generated by the plasma treatments, as shown by the reduction in I_p in Figs. 6 and 12. So, the microstructure is not strongly distorted and not like a disordered structure as formed by the plasma treatments. Because of this, the diffusion of H atoms to terminate the DBs is relatively restricted, and thus E_a is large.

For the annihilation of the photon-induced defects, we find that the preexponential factor k_0 is different between the UV- and VUV-photon-induced defects, even though E_a is nearly the same them, as shown in Fig. 3. Correspondingly, the recovery time (i.e., τ) is different depending on the photon energy; τ is greater for the VUV-photon-induced defects. A possible explanation for this is shown in Fig. 19. As is known, photon absorption in *a*-Si:H film creates excited states locally, which results in breaking of the Si—H bond. The broken bond (i.e., DB) and the released H atom are expected to be close to each other, as shown in Fig. 19(a). However, the location of H atoms may differ depending on the excess energy of the H atom. A higher photon energy results in a larger excess energy of the H atom, which may drive the diffusion of the released H atom or the deformation of the local structure, as in Fig. 19(b). In such a case, the released H atoms take longer to diffuse back to the bond-breaking sites to terminate the DB defects. Also, the restoration of the locally deformed structure is expected to take an additional period. Therefore, the

recovery time is longer for the defects generated by VUV photons.

VI. CONCLUSIONS

We investigate the kinetics of electronic defects in *a*-Si:H films during H_2- and Ar-plasma treatments, and postannealing. The generation and annihilation of the electronic defects (i.e, the silicon DBs) are monitored via *in situ* photocurrent measurements. The defects are generated by each plasma treatment, which is indicated by a strong reduction in the photocurrent. The dominant species responsible for the generation of defects are found to be radicals such as H radicals for H_2 plasmas and Ar^* radicals for Ar plasmas. To distinguish the effects of photons, radicals, and ions on the generation of defects, the *a*-Si:H film surface is exposed selectively to these species with use of samples of different structures. The Ar^+-ion bombardment is found to create the residual defects, and the amount of the residual defects increases with the treatment time. For photon irradiation, the generation of defects is dependent on the photon energy, photon flux, and irradiation period. UV photons generate defects more efficiently than visible photons. Defect generation by VUV photons is even more pronounced.

After the photon, radical, or plasma treatment, the defects in *a*-Si:H films are annihilated partially or completely by postannealing, which is indicated by the recovery of the photocurrent. The photon- and radical-induced defects are recovered completely by simple postannealing. However, Ar^+-ion-created residual defects require an additional H_2-plasma treatment and postannealing to mostly remove them. A beneficial effect of H atoms for defect annihilation is thus experimentally demonstrated.

The recovery of the photocurrent (i.e., the annihilation of defects) exhibited dispersive behavior. The characteristic time for the annihilation of defects is determined from a fit with a stretched exponential term. An Arrhenius plot (i.e., $1/\tau$ vs $1/T$) is obtained for the photon- and plasma-induced defects. The experimentally obtained $1/\tau$ shows an exponential decay with $1/T$, indicating that a thermal activation process plays an important role in defect annihilation. We find that the activation energy is dependent on the origin of the defect generation. The activation energy E_a is 0.53 ± 0.06 eV for plasma-induced defects and 1.17 ± 0.06 eV for photon-induced defects. This result implies microstructural disordering of the defect-rich surface layer formed with the plasma treatments, where mobile H atoms can diffuse easily through a rarefied/porous local network structure.

ACKNOWLEDGMENTS

The authors are grateful to Professor M. Shiratani (Kyushu University), Professor K. Koga (Kyushu University), and Dr. C. McDonald (National Institute of Advanced Industrial Science and Technology) for valuable discussions. This work was supported in part by JSPS KAKENHI (Grants No. 18K03603 and No. 15K04717).

[1] S. M. Sze and K. K. Ng, *Physics of Semiconductor Devices* (Wiley-Interscience, Hoboken, NJ, 2007), 3rd ed.
[2] D. K. Schroder, *Semiconductor Material and Device Characterization* (John Wiley, Chichester, 2006).
[3] A. Martin, Review on the reliability characterization of plasma-induced damage, J. Vac. Sci. Technol. B **27**, 426 (2009).
[4] K. Eriguchi and K. Ono, Quantitative and comparative characterizations of plasma process-induced damage in advanced metal-oxide-semiconductor devices, J. Phys. D **41**, 024002 (2008).
[5] M. Ceschia, A. Paccagnella, A. Cester, A. Scarpa, and G. Ghidini, Radiation induced leakage current and stress induced leakage current in ultra-thin gate oxides, IEEE Trans. Nucl. Sci. **45**, 2375 (1998).
[6] M. J. Powell, Charge trapping instabilities in amorphous silicon-silicon nitride thin-film transistors, Appl. Phys. Lett. **43**, 597 (1983).
[7] W. G. J. H. M. van Sark, L. Korte, and F. Roca, *Physics and Technology of Amorphous-Crystalline Heterostructure Silicon Solar Cells* (Springer-Verlag, Berlin, 2012).
[8] S. D. Wolf, A. Descoeudres, Z. C. Holman, and C. Ballif, High-efficiency silicon heterojunction solar cells: A review, Green **2**, 7 (2012).
[9] G. S. Oehrlein, Dry etching damage of silicon: A review, Mater. Sci. Eng. B **4**, 441 (1989).
[10] K. P. Cheung, *Plasma Charging Damage* (Springer, Heidelberg, 2001).
[11] K. Eriguchi, Defect generation in electronic devices under plasma exposure: Plasma-induced damage, Jpn. J. Appl. Phys. **56**, 06HA01 (2017).
[12] Z. Q. Ma, Y. F. Zheng, and B. X. Liu, Ion-induced surface and bulk displacement threshold for epitaxial growth, Phys. Stat. Sol. (a) **169**, 239 (1998).
[13] T. Ohchi, S. Kobayashi, M. Fukasawa, K. Kugimiya, T. Kinoshita, T. Takizawa, S. Hamaguchi, Y. Kamide, and T. Tatsumi, Reducing damage to Si substrates during gate etching processes, Jpn. J. Appl. Phys. **47**, 5324 (2008).
[14] A. H. M. Smets, W. M. M. Kessels, and M. C. M. vandeSanden, The effect of ion-surface and ion-bulk interactions during hydrogenated amorphous silicon deposition, J. Appl. Phys. **102**, 073523 (2007).
[15] N. Yabumoto, M. Oshima, O. Michikami, and S. Yoshii, Surface damage on Si substrates caused by reactive sputter etching, Jpn. J. Appl. Phys. **20**, 893 (1981).
[16] T. Tatsumi, S. Fukuda, and S. Kadomura, Radiation damage of SiO_2 surface induced by vacuum ultraviolet photons of high-density plasma, Jpn. J. Appl. Phys. **33**, 2175 (1994).
[17] J. Kanicki, W. L. Warren, C. H. Seager, M. S. Crowder, and P. M. Lenahan, Microscopic origin of the light-induced defects in hydrogenated nitrogen-rich amorphous silicon nitride films, J. Non-Cryst. Solids **137**, 291 (1991).
[18] J. Lee and D. B. Graves, The effect of VUV radiation from Ar/O_2 plasmas on low-k SiOCH films, J. Phys. D: Appl. Phys. **44**, 325203 (2011).

[19] S. Yasuhara, J. Chung, K. Tajima, H. Yano, S. Kadomura, M. Yoshimaru, N. Matsunaga, and S. Samukawa, Impact of film structure on damage to low-k SiOCH film during plasma exposure, J. Phys. D: Appl. Phys. **42**, 235201 (2009).

[20] J. Perrin, O. Rosny, and M. C. Bordage, Cross-sections, rate constants and transport coefficients in silane plasma chemistry, Contrib. Plasma Phys. **36**, 3 (1996).

[21] A. Matsuda, Microcrystalline silicon: Growth and device application, J. Non-Cryst. Solids **338**, 1 (2004).

[22] S. Ramalingam, D. Maroudas, E. S. Aydil, and S. P. Walch, Abstraction of hydrogen by SiH_3 from hydrogen-terminated Si(001)-(2 × 1) surfaces, Surf. Sci. **418**, L8 (1998).

[23] T. Hayashi, K. Ishikawa, M. Sekine, and M. Hori, Computational study on SiH_4 dissociation channels and H abstraction reactions, Jpn. J. Appl. Phys. **55**, 07LD07 (2016).

[24] K. Koga, T. Inoue, K. Bando, S. Iwashita, M. Shiratani, and Y. Watanabe, Highly stable a-Si:H films deposited by using multi-hollow plasma chemical vapor deposition, Jpn. J. Appl. Phys. **44**, L1430 (2005).

[25] S. Nunomura, K. Koga, M. Shiratani, Y. Watanabe, Y. Morisada, N. Matsuki, and S. Ikeda, Fabrication of nanoparticle composite porous films having ultralow dielectric constant, Jpn. J. Appl. Phys. **44**, L1509 (2005).

[26] D. Abou-Ras, T. Kirchartz, and U. Rau, *Advanced Characterization Techniques for Thin Film Solar Cells* (Wiley-VCH, Weinheim, 2011).

[27] Y. Nakakubo, K. Eriguchi, and K. Ono, Characterization of plasma process-induced latent defects in surface and interface layer of Si substrate, ECS J. Solid State Sci. Technol. **4**, N5077 (2015).

[28] A. S. Yapsir, P. Hadizad, T.-M. Lu, J. C. Corelli, J. W. Corbett, W. A. Lanford, and H. Bakhru, Defect centers and changes in the electrical characteristics of Al/n-type Si Schottky diodes induced by hydrogen-ion implantations, Phys. Rev. B **37**, 8982 (1988).

[29] D. V. Lang, J. D. Cohen, and J. P. Harbison, Measurement of the density of gap states in hydrogenated amorphous silicon by space charge spectroscopy, Phys. Rev. B **25**, 5285 (1982).

[30] S. Yamasaki, U. K. Das, and T. Yasuda, Fast hydrogen diffusion in hydrogenated amorphous silicon observed by in situ ESR, J. Non-Cryst. Solids **299**, 185 (2002).

[31] U. K. Das, T. Yasuda, and S. Yamasaki, In situ ESR study to detect the diffusion of free H and creation of dangling bonds in hydrogenated amorphous silicon, Phys. Rev. B **63**, 245204 (2001).

[32] U. K. Das, T. Yasuda, and S. Yamasaki, Fast Diffusion of H and Creation of Dangling Bonds in Hydrogenated Amorphous Silicon Studied by in Situ ESR, Phys. Rev. Lett. **85**, 2324 (2000).

[33] Y. Ishikawa, Y. Ichihashi, S. Yamasaki, and S. Samukawa, Generation and reduction in SiO_2/Si interface state density during plasma etching processes, J. Appl. Phys. **104**, 063308 (2008).

[34] S. Lee, M. Gunes, C. R. Wronski, N. Maley, and M. Bennett, Effect of midgap states in intrinsic hydrogenated amorphous silicon on sub-band-gap photoconductivity, Appl. Phys. Lett. **59**, 1578 (1991).

[35] N. Wyrsch, F. Finger, T. J. McMahon, and M. Vanecek, How to reach more precise interpretation of subgap absorption spectra in terms of deep defect density in a-Si:H, J. Non-Cryst. Solids **137**, 347 (1991).

[36] I. Sakata, M. Yamanaka, S. Numase, and Y. Hayashi, Deep defect states in hydrogenated amorphous silicon studied by a constant photocurrent method, J. Appl. Phys. **71**, 4344 (1992).

[37] M. Vanecek, J. Kocka, A. Poruba, and A. Fejfar, Direct measurement of the deep defect density in thin amorphous silicon films with the "absolute" constant photocurrent method, J. Appl. Phys. **78**, 6203 (1995).

[38] G. S. Oehrlein, A. A. Bright, and S. W. Robey, X-ray photoemission spectroscopy characterization of silicon surfaces after CF_4/H_2 magnetron ion etching: Comparisons to reactive ion etching, J. Vac. Sci. Technol. A **6**, 1989 (1988).

[39] M. Schmidt, A. Schoepke, O. Milch, Th. Lussky, and W. Fuhs, Photoelectron spectroscopic investigations of very thin a-Si:H layers, Mat. Res. Soc. Symp. **762**, 125 (2003).

[40] R. A. Street, *Hydrogeneted Amorphous Silicon* (Cambridge University Press, Cambridge, 1991).

[41] K. Tanaka, E. Maruyama, T. Shimada, and H. Okamoto, *Amorphous Silicon* (John Wiley, Chichester, 1999).

[42] A. H. M. Smets, W. M. M. Kessels, and M. C. M. van de Sanden, Vacancies and voids in hydrogenated amorphous silicon, Appl. Phys. Lett. **82**, 1547 (2003).

[43] A. H. M. Smets and M. C. M. van de Sanden, Relation of the Si-H stretching frequency to the nanostructural Si-H bulk environment, Phys. Rev. B **76**, 073202 (2007).

[44] H. C. Neitzert, W. Hirsch, and M. Kunst, In situ process evaluation during hydrogen plasma etching of a-Si:H films by microwave detected transient photoconductivity measurements, J. Appl. Phys. **73**, 7446 (1993).

[45] H. C. Neitzert and M. Kunst, In situ measurements of the recombination at the crystalline silicon/amorphous silicon heterointerface by time resolved microwave conductivity measurements during low temperature annealing and silane plasma exposure, J. Vac. Sci. Technol. A **13**, 2753 (1995).

[46] I. M. P. Aarts, B. Hoex, A. H. M. Smets, R. Engeln, W. M. M. Kessels, and M. C. M. van de Sanden, Direct and highly sensitive measurement of defect-related absorption in amorphous silicon thin films by cavity ringdown spectroscopy, Appl. Phys. Lett. **84**, 3079 (2004).

[47] F. J. J. Peeters, J. Zheng, I. M. P. Aarts, A. C. R. Pipino, W. M. M. Kessels, and M. C. M. van de Sanden, Atomic hydrogen induced defect kinetics in amorphous silicon, J. Vac. Sci. Technol. A **35**, 05C307 (2017).

[48] S. Nunomura, I. Sakata, and M. Kondo, In situ photocurrent measurements of thin-film semiconductors during plasma-enhanced chemical vapor deposition, Appl. Phys. Express **6**, 126201 (2013).

[49] S. Nunomura and I. Sakata, In-situ characterization of trapped charges in amorphous semiconductor films during plasma-enhanced chemical vapor deposition, AIP Adv. **4**, 097110 (2014).

[50] S. Nunomura, X. Che, and S. R. Forrest, Charge trapping in mixed organic donor-acceptor semiconductor thin films, Adv. Mater. **26**, 7555 (2014).

[51] S. Uchida, S. Takashima, M. Hori, M. Fukasawa, K. Ohshima, K. Nagahata, and T. Tatsumi, Plasma damage

mechanisms for low-k porous SiOCH films due to radiation, radicals, and ions in the plasma etching process, J. Appl. Phys. **103**, 073303 (2008).

[52] K. Takeda, Y. Miyawaki, S. Takashima, M. Fukasawa, K. Oshima, K. Nagahata, T. Tatsumi, and M. Hori, Mechanism of plasma-induced damage to low-k SiOCH films during plasma ashing of organic resists, J. Appl. Phys. **109**, 033303 (2011).

[53] R. H. Bube, *Photoconductivity of Solids* (John Wiley, New York, 1960).

[54] R. H. Bube, *Photoelectronic Properties of Semiconductors* (Cambridge University Press, Cambridge, 1992).

[55] J. A. Schmidt, R. Arce, R. H. Buitrago, and R. R. Koropecki, Light-induced defects in hydrogenated amorphous silicon studied by the constant-photocurrent method, Phys. Rev. B **55**, 9621 (1997).

[56] G. Bruno, P. Capezzuto, and A. Madan, *Plasma Deposition of Amorphous Silicon-Based Materials* (Academic Press, San Diego, 1995).

[57] S. Nunomura and M. Kondo, Characterization of high-pressure capacitively coupled hydrogen plasmas, J. Appl. Phys. **102**, 093306 (2007).

[58] S. Nunomura, I. Yoshida, and M. Kondo, Transient phenomena in plasma-enhanced chemical vapor deposition processes of thin-film silicon, Jpn. J. Appl. Phys. **49**, 106102 (2010).

[59] S. Nunomura, I. Sakata, and K. Matsubara, Electronic properties of ultrathin hydrogenated amorphous silicon, Appl. Phys. Express **10**, 081401 (2017).

[60] S. Nunomura, I. Sakata, and K. Matsubara, Impact of band tail distribution on carrier trapping in hydrogenated amorphous silicon for solar cell applications, J. Non-Cryst. Solids **44**, 436 (2016).

[61] H. Fujiwara, *Spectroscopic Ellipsometry: Principles and Applications* (John Wiley & Sons Ltd, Chichester, 2007).

[62] G. E. Jellison and F. A. Modine, Parameterization of the optical functions of amorphous materials in the interband region, Appl. Phys. Lett. **69**, 371 (1996) [Erratum **69**, 2137 (1996)].

[63] S. Nunomura and M. Kondo, Precursor flux-dependent microstructure of thin-film silicon prepared by hydrogen diluted silane discharge plasmas, J. Phys. D: Appl. Phys. **42**, 185210 (2009).

[64] J. Hopwood, C. R. Guarnieri, S. J. Whitehair, and J. J. Cuomo, Langmuir probe measurements of a radio frequency induction plasma, J. Vac. Sci. Technol. A, **11**, 152 (1998).

[65] S. Takashima, M. Hori, T. Goto, A. Kono, M. Ito, and K. Yoneda, Vacuum ultraviolet absorption spectroscopy employing a microdiacharge hollow-cathode lamp for absolute density measurements of hydrogen atoms in reactive plasmas, Appl. Phys. Lett. **75**, 3929 (1999).

[66] S. Nunomura, H. Katayama, and I. Yoshida, Hydrogen atom kinetics in capacitively coupled plasmas, Plasma Sources Sci. Technol. **26**, 055018 (2017).

[67] K. Sawada and T. Fujimoto, Effective ionization and dissociation rate coefficients of molecular hydrogen in plasma, J. Appl. Phys. **78**, 2913 (1995).

[68] H. Tawara, Y. Itikawa, H. Nishimura, and M. Yoshino, Cross sections and related data for electron collisions with hydrogen molecules and molecular ions, J. Chem. Phys. Dara **19**, 617 (2009).

[69] D. Redfield and R. H. Bube, *Photoinduced Defects in Semiconductors* (Cambridge University Press, New York, 1996).

[70] J. Kakalios, R. A. Street, and W. B. Jackson, Stretched-Exponential Relaxation Arising from Dispersive Diffusion of Hydrogen in Amorphous Silicon, Phys. Rev. Lett. **59**, 1037 (1987).

[71] J. H. Yoon, Y. Z. Lee, and H. R. Park, Thermal relaxation of the deposition-induced nonequilibrium state and steady-state defect density in hydrogenated amorphous silicon, Phys. Rev. B **49**, 10303 (1994).

[72] A. Bogaerts and R. Gijbels, Modeling of metastable argon atoms in a direct-current glow discharge, Phys. Rev. A **52**, 3743 (1995).

[73] R. A. Street, C. C. Tsai, J. Kakalios, and W. B. Jackson, Hydrogen diffusion in amorphous silicon, Philos. Mag. B **56**, 305 (1987).

[74] W. Beyer and H. Wagner, Determination of the hydrogen diffusion coefficient in hydrogenated amorphous silicon from hydrogen effusion experiments, J. Appl. Phys. **53**, 8745 (1982).

[75] H. Ohta and S. Hamaguchi, Molecular dynamics simulation of silicon and silicon dioxide etching by energetic halogen beams, J. Vac. Sci. Technol. A **19**, 2373 (2001).

[76] M. Fukasawa, Y. Nakakubo, A. Matsuda, Y. Takao, K. Eriguchi, K. Ono, M. Minami, F. Uesawa, and T. Tatsumi, Structural and electrical characterization of HBr/O_2 plasma damage to Si substrate, J. Vac. Sci. Technol. A **29**, 041301 (2011).

[77] F. Kail, A. Fontcuberta, I. Morral, A. Hadjadj, P. Roca, I. Cabarrocas, and A. Beorchia, Hydrogen-plasma etching of hydrogenated amorphous silicon: A study by a combination of spectroscopic ellipsometry and trap-limited diffusion model, Phylos. Mag. **84**, 595 (2004).

[78] K. Hattori, H. Okamoto, and Y. Hamakawa, Theory of the steady-state-photocarrier-grating technique for obtaining accurate diffusion-length measurements in amorphous silicon, Phys. Rev. B **45**, 1126 (1992).

[79] J. D. Cohen, Light-induced defects in hydrogenated amorphous silicon germanium alloys, Sol. Energy Mater. Sol. Cells **78**, 399 (2003).

[80] H. R. Park, J. Z. Liu, and S. Wagner, Saturation of the light-induced defect density in hydrogenated amorphous silicon, Appl. Phys. Lett. **55**, 2658 (1989).

[81] H. Dersch, J. Stuke, and J. Beichler, Light-induced dangling bonds in hydrogenated amorphous silicon, Appl. Phys. Lett. **38**, 456 (1981).

[82] C. G. V. de Walle, Energies of various configurations of hydrogen in silicon, Phys. Rev. B **49**, 4579 (1998).

[83] H. Tanimoto, H. Arai, H. Mizubayashi, M. Yamanaka, and I. Sakata, Light-induced hydrogen evolution from hydrogenated amorphous silicon: Hydrogen diffusion by formation of bond centered hydrogen, J. Appl. Phys. **115**, 073503 (2014).

[84] M. Stutzmann, W. B. Jackson, and C. C. Tsai, Light-induced metastable defects in hydrogenated amorphous silicon: A systematic study, Phys. Rev. B **32**, 23 (1985).